electronic reprint

JOURNAL OF APPLIED CRYSTALLOGRAPHY

ISSN: 1600-5767
journals.iucr.org/j

Inverse pole figure mapping of bulk crystalline grains in a polycrystalline steel plate by pulsed neutron Bragg-dip transmission imaging

Hirotaka Sato, Yoshinori Shiota, Satoshi Morooka, Yoshikazu Todaka, Nozomu Adachi, Sunao Sadamatsu, Kenichi Oikawa, Masahide Harada, Shuoyuan Zhang, Yuhua Su, Takashi Kamiyama, Masato Ohnuma, Michihiro Furusaka, Takenao Shinohara and Yoshiaki Kiyanagi

J. Appl. Cryst. (2017). **50**, 1601–1610

JOURNAL OF APPLIED CRYSTALLOGRAPHY
ISSN 1600-5767

Inverse pole figure mapping of bulk crystalline grains in a polycrystalline steel plate by pulsed neutron Bragg-dip transmission imaging

Hirotaka Sato,[a]* Yoshinori Shiota,[b] Satoshi Morooka,[c] Yoshikazu Todaka,[d] Nozomu Adachi,[d] Sunao Sadamatsu,[e] Kenichi Oikawa,[f] Masahide Harada,[f] Shuoyuan Zhang,[g] Yuhua Su,[f] Takashi Kamiyama,[a] Masato Ohnuma,[a] Michihiro Furusaka,[a] Takenao Shinohara[f] and Yoshiaki Kiyanagi[b]

[a]Faculty of Engineering, Hokkaido University, Kita-13 Nishi-8, Kita-ku, Sapporo, Hokkaido 060-8628, Japan, [b]Graduate School of Engineering, Nagoya University, Furo-cho, Chikusa-ku, Nagoya, Aichi 464-8603, Japan, [c]Materials Sciences Research Center, Japan Atomic Energy Agency (JAEA), 2-4 Shirakata, Tokai, Naka, Ibaraki 319-1195, Japan, [d]Department of Mechanical Engineering, Toyohashi University of Technology, 1-1 Hibarigaoka, Tempaku-cho, Toyohashi, Aichi 441-8580, Japan, [e]Graduate School of Science and Engineering, Kagoshima University, 1-21-40 Korimoto, Kagoshima, 890-0065, Japan, [f]J-PARC Center, Japan Atomic Energy Agency (JAEA), 2-4 Shirakata, Tokai, Naka, Ibaraki 319-1195, Japan, and [g]Neutron Science and Technology Center, Comprehensive Research Organization for Science and Society (CROSS), 162-1 Shirakata, Tokai, Naka, Ibaraki 319-1106, Japan. *Correspondence e-mail: h.sato@eng.hokudai.ac.jp

Received 1 April 2017
Accepted 10 September 2017

Edited by A. Borbély, Ecole National Supérieure des Mines, Saint-Etienne, France

Keywords: pulsed neutron Bragg-dip transmission imaging; grain orientation mapping; inverse pole figures; large-area bulk analysis.

A new mapping procedure for polycrystals using neutron Bragg-dip transmission is presented. This is expected to be useful as a new materials characterization tool which can simultaneously map the crystallographic direction of grains parallel to the incident beam. The method potentially has a higher spatial resolution than neutron diffraction imaging. As a demonstration, a Bragg-dip neutron transmission experiment was conducted at J-PARC on beamline MLF BL10 NOBORU. A large-grained Si–steel plate was used. Since this specimen included multiple grains along the neutron beam transmission path, it was a challenging task for existing methods to analyse the direction of the crystal lattice of each grain. A new data-analysis method for Bragg-dip transmission measurements was developed based on database matching. As a result, the number of grains and their crystallographic direction along the neutron transmission path have been determined.

1. Introduction

Mapping of crystalline grains and their orientation is a powerful methodology to investigate the correlation between the properties of a material and its microstructure. For example, scanning electron microscopy electron backscatter diffraction (SEM-EBSD) (Humphreys, 2004) and X-ray diffraction (XRD) imaging (Ludwig *et al.*, 2008; Johnson *et al.*, 2008) are frequently used for grain orientation mapping. SEM-EBSD can map grain orientation with sub-micrometre spatial resolution, but it is restricted to near-surface and local-area analysis of a specimen. XRD imaging can non-destructively map grain orientation with a spatial resolution of the order of micrometres in three-dimensional real space. Incidentally, a grain orientation map obtained by XRD imaging (diffraction contrast) is often overlaid on and complimented by an absorption/phase-contrast X-ray transmission image (Ludwig *et al.*, 2009).

Neutrons have a higher material penetration ability than electrons or X-rays. Therefore, analyses of bulk-averaged (high statistical reliability) information on crystalline phases such as crystallographic texture, crystallite size and lattice strain in centimetre-sized polycrystalline materials are

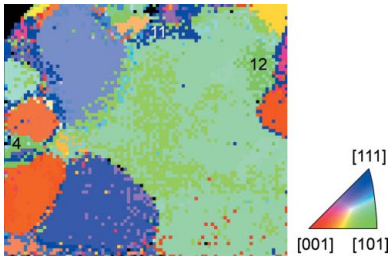

performed by neutron diffraction [*e.g.* texture analysis (Wenk *et al.*, 2003), strain analysis (Santisteban *et al.*, 2006) and phase analysis (Gutmann *et al.*, 2006)] and Bragg-edge neutron transmission imaging [*e.g.* strain analysis/imaging (Santisteban *et al.*, 2002), texture/crystallite-size analysis/imaging (Sato *et al.*, 2011) and phase analysis/imaging (Woracek *et al.*, 2014)]. Recently, development projects for neutron diffraction imaging were launched using both continuous (Peetermans *et al.*, 2014) and pulsed neutron sources (Cereser *et al.*, 2017) for crystal orientation analysis.

We are developing a grain orientation mapping method based on pulsed neutron Bragg-dip transmission imaging, rather than using the neutron diffraction imaging approach utilized by previous researchers. The reasons are as follows. Firstly, (pulsed) neutron (Bragg-edge/dip) transmission imaging is expected to have higher spatial resolution ability (Tremsin *et al.*, 2012; Sato, Sato *et al.*, 2015; Sato, Shiota *et al.*, 2015) than neutron diffraction imaging (Gutmann *et al.*, 2006). It also benefits from the pulsed neutron transmission imaging instruments with low beam angular divergence that have been constructed recently, utilizing intense pulsed spallation sources, such as the J-PARC beamline MLF BL22 RADEN (Shinohara *et al.*, 2016), the Rutherford Appleton Laboratory ISIS beamline IMAT (Kockelmann *et al.*, 2013) and the European Spallation Source beamline ODIN (Strobl, 2015). Furthermore, significant progress has been made recently in the development of high-spatial-resolution (about 55 µm) two-dimensional detectors for pulsed neutron transmission imaging (Tremsin *et al.*, 2012). The large field of view (∼10 × 10 cm) with a spatial resolution of a few hundred micrometres is one of the features of neutron transmission imaging. Secondly, crystal orientation analysis using a neutron transmission method (such as pulsed neutron Bragg-dip transmission spectroscopy, which is usually applied to single-crystal-type materials; Santisteban, 2005; Kockelmann *et al.*, 2007; Malamud & Santisteban, 2016) is convenient because the neutron wavelengths of Bragg dips can reflect the crystal orientation of the single crystal. This is because the Bragg dip appears at the neutron wavelength $\lambda = 2d\sin\theta$, where d is the crystal-lattice plane spacing and θ is the Bragg angle. In fact, whole-pattern least-squares fitting analysis of a Bragg-dip transmission spectrum has already been developed for crystallographic parameter refinement of single-crystal materials (*e.g.* crystal-lattice parameters, crystal orientation, crystal mosaicity, strain *etc.*) by Malamud & Santisteban (2016). However, the determination of the orientation of a single crystallite in a material containing overlapping grains is quite difficult for least-squares Bragg-dip pattern fitting/refinement without a rough initial estimation of the crystallographic parameters of each single crystal included in the neutron transmission path. Since the wavelength positions of narrow Bragg dips are easily changed by the crystal orientation (Santisteban, 2005; Malamud & Santisteban, 2016), least-squares fitting algorithms cannot follow such a mathematically discontinuous profile. These difficulties mean that grain orientation mapping of a polycrystalline material using Bragg-dip transmission spectra requires a new data-analysis approach which can rapidly determine the number of grains and their orientation along the neutron transmission path.

In this paper we present such a new data-analysis method, referred to here as the database matching method for the Bragg-dip transmission spectrum. This new method can rapidly determine the number of grains and the direction of the crystal lattice lying parallel to the neutron beam direction, although the crystal orientation cannot be completely determined. This is because the direction of the crystal lattice along the transverse direction can differ by a rotation around the beam direction and therefore cannot be identified by the present method. We also present the results of grain orientation mapping, in particular inverse pole figures (IPFs), of grains of a bulk polycrystalline steel specimen. Finally, we compare and evaluate the results of neutron transmission IPF mapping with EBSD results.

2. Experimental

2.1. Specimen

Fig. 1 shows images of the investigated specimen, which is an Si–steel plate of 5 mm thickness, 6.90 cm height and 6.75 cm width, used for electromagnetic applications. The

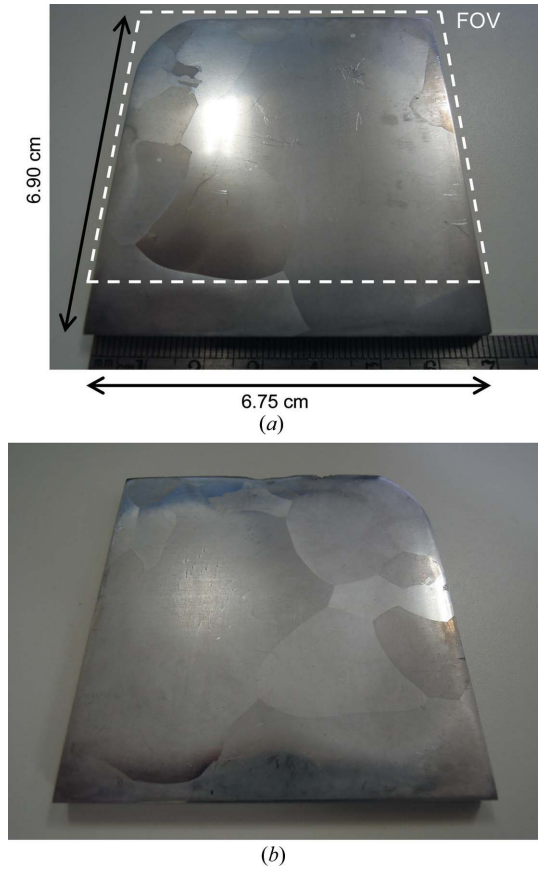

Figure 1
Photographs of a 3.4mass% Si–steel specimen containing large grains. The plate thickness is 5 mm. Panel (*a*) is an image of one side of the plate and panel (*b*) shows the other side. The region surrounded by dashed white lines indicates the field of view (FOV).

crystal structure is body-centred cubic (b.c.c.). Grain boundaries can be observed on the surface with the naked eye (see Fig. 1). The grains have sizes that range from approximately a millimetre to several centimetres. The grain shapes observed on one side (Fig. 1*a*) are slightly different from those observed on the reverse side (Fig. 1*b*). Therefore, it is likely that there are regions where two or more stacked grains exist along the normal direction of the plate.

This large-grained material was chosen for the first demonstration of neutron transmission IPF mapping, restricted by the pixel size (800 µm) of the pulsed neutron imaging detector used in this study.

2.2. Pulsed neutron source, beamline and imaging detector

Fig. 2 shows a schematic of the layout of the pulsed neutron transmission imaging experiment. The experiment was performed on the Neutron Beamline for Observation and Research Use (NOBORU) (Oikawa *et al.*, 2008) on BL10 of the Materials and Life Science Experimental Facility (MLF) at the Japan Proton Accelerator Research Complex (J-PARC). NOBORU views the decoupled-type 20 K supercritical 100%-para-H_2 moderator of the Japan Spallation Neutron Source (JSNS) driven by a 3 GeV proton synchrotron. The pulse repetition rate of the proton accelerator was 25 Hz. The moderator surface area was 10 × 10 cm. The proton beam power was 400 or 500 kW during this experiment. The neutron pulse FWHM was about 50 µs for cold neutrons (0.4 nm wavelength). Thus, the wavelength resolution of the time-of-flight (TOF) analysis at the detector position, 14.26 m from the moderator surface, was about 0.35% for cold neutrons, sufficient to observe Bragg dips (see Fig. 3).

The size of the neutron slit at 7.05 m from the moderator surface was 3 × 3 mm. This slit size also determined the beam intensity and the beam divergence. The sample was set at 14.22 m and the detector at 14.26 m. Thus, the neutron beam divergence was about 0.416 mrad (the collimator ratio *L*/*D* was about 2400). The umbra beam size at the detector (14.26 m) was about 9.62 × 9.62 cm. The estimated thermal/cold neutron flux when the proton beam power was 500 kW was about 8×10^4 n cm^{-2} s^{-1}. This flux was chosen to keep the count rate just below the saturation limit of the detector. A wavelength bandwidth chopper positioned at 7.2 m was used to prevent frame overlap between the slow neutrons of a certain pulse and the fast neutrons of the next pulse. The wavelength bandwidth was about 0.9 nm.

The neutron imaging detector with the TOF analysis function used here was a gas electron multiplier (GEM) detector (Uno *et al.*, 2012). The GEM detector is one of the best high-spatial-resolution neutron counting-type detectors and is frequently used for pulsed neutron transmission imaging. The pixel size was 800 × 800 µm, giving an active area of 10.24 × 10.24 cm for the 128 × 128 pixels. The detector was set 4 cm behind the specimen. The time bin width was 10 µs. The averaged neutron counting rate of the detector during this experiment was 1.6×10^3 n cm^{-2} s^{-1}, which was almost at the limit of the counting rate of the detector (about

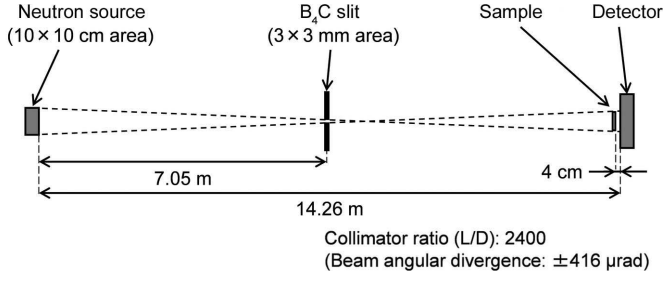

Figure 2
Schematic of the experimental layout of a pulsed neutron transmission imaging setup.

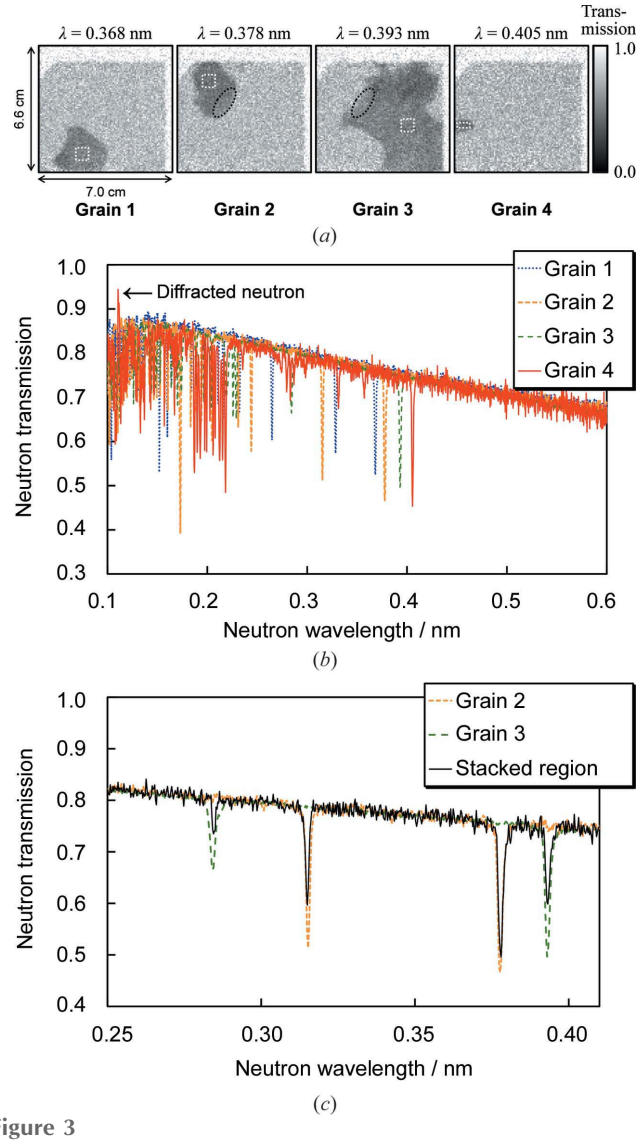

Figure 3
(*a*) Wavelength-dependent neutron transmission images detecting Grains 1, 2, 3 and 4. (*b*) Area-integrated neutron transmission spectra including Bragg dips caused by single-crystallite diffraction at the positions of Grains 1, 2, 3 and 4. The corresponding regions are indicated by white dashed lines in panel (*a*). (*c*) Neutron transmission spectra of Grains 2 and 3 (white dashed lines) and the stacked region of both Grain 2 and Grain 3, which is the area surrounded by black dashed lines in panel (*a*).

3×10^3 n cm^{-2} s^{-1}). The detection efficiency was of the order of several percent.

The measurement time was about 7.2 h for an open-beam measurement and about 14.5 h for the sample measurement. This long time was required because of the limitation in the count rate.

3. Results of transmission images and Bragg-dip neutron transmission spectra

Figs. 3(*a*) and 3(*b*) show, respectively, wavelength-dependent neutron transmission images and position-dependent neutron transmission spectra, including Bragg dips caused by single-crystal diffraction. Four grains were recognized. Fig. 4 indicates a schematic view of diffraction by grains having different orientations. It is known that the orientation of a grain is related to the Bragg-dip wavelength $\lambda = 2d\sin\theta$ derived from the Bragg angle θ. Thus, Figs. 3(*a*) and 3(*b*) reflect the fact that the Bragg-dip wavelengths differ owing to differences in the crystal orientation of each grain. Therefore, from the Bragg-dip wavelengths the crystal orientation of each grain can be deduced. Note that for certain wavelengths the recorded neutron intensity shows peaks that are caused by neutrons being diffracted from the sample in the forward direction and still recorded on the detector (see Fig. 3*b*). This signal interferes as noise with our target data, mainly up to a wavelength of ~0.287 nm, where no more neutrons are diffracted to angles smaller than $\theta = 45^\circ$ for b.c.c. Fe.

Fig. 3(*c*) shows neutron transmission spectra for Grains 2 and 3 and the stacked region of both Grain 2 and Grain 3, indicated by the dashed-line ellipses in Fig. 3(*a*). In the stacked region the transmission spectrum is composed of Bragg-dip patterns from both Grain 2 and Grain 3. We took such effects into consideration when we analysed the data.

4. A fast determination method for the number of grains and their crystal-lattice directions along the neutron-beam transmission path

For a fast determination of the number of grains along the neutron beam direction, a new method for analysis of the Bragg-dip transmission spectrum obtained from multiple grains stacked along that direction was developed. The algorithm consists of three parts: (i) analysis of the Bragg-dip wavelengths from experimental data; (ii) a database of various Bragg-dip patterns depending on the crystal-lattice direction along the neutron beam direction; and (iii) a system matching the experimental data to the database.

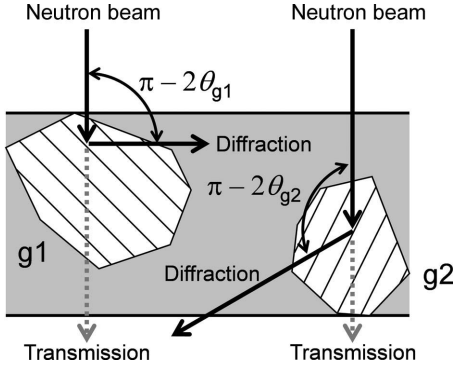

Figure 4
Schematic view indicating the difference in Bragg-dip wavelengths. Different grain orientations lead to different Bragg angles θ and different Bragg-dip wavelengths $\lambda = 2d\sin\theta$.

4.1. Analysis of Bragg-dip wavelengths

Fig. 5(*a*) shows an experimental Bragg-dip transmission spectrum Tr_{exp}, together with a fitted curve $Tr_{nonBragg}$. A Bragg-dip transmission spectrum Tr_{exp} consists not only of the coherent elastic (Bragg) scattering component Tr_{dip} but also of non-Bragg scattering (the incoherent elastic scattering, the inelastic scattering and the absorption) $Tr_{nonBragg}$. For the extraction of the Bragg scattering component Tr_{dip} only, we first determined a TOF-dependent function of $Tr_{nonBragg}$ using high-statistics experimental data (area-integrated data for Grain 3). As a result,

$$Tr_{nonBragg}(t) = 0.96242 \exp\left(-1.8305 \times 10^{-5} t\right) \quad (1)$$

was derived by least-squares fitting using baseline data for non-Bragg scattering in Tr_{exp} over the wavelength region from 0.25 to 0.5 nm. Here, t is the neutron flight time (in microseconds) from the neutron source to the detector, which is a function of the neutron wavelength λ. In principle, under the same conditions of chemical composition and sample thickness, $Tr_{nonBragg}$ is independent of the grain position in the sample.

Then, the Bragg scattering component Tr_{dip} was extracted from the experimental data Tr_{exp} using the following equation:

$$Tr_{dip}[\lambda(t)] = \frac{Tr_{exp}[\lambda(t)]}{Tr_{nonBragg}[\lambda(t)]}. \quad (2)$$

Next, Tr_{dip} was converted from transmission-rate (dip-like) data Tr_{dip} to attenuation-rate (peak-like) data R_{dip} [corresponding to the Bragg-reflected attenuation R defined by Malamud & Santisteban (2016)], using the following equation:

$$R_{dip}(\lambda) = 1 - Tr_{dip}(\lambda). \quad (3)$$

Figs. 5(*b*) and 5(*c*) show this conversion procedure using one-pixel data. Here, however, the one-pixel data have quite a low statistical reliability. It is not so easy for automatic analysis of Bragg-dip data measured at many pixels to identify Bragg-dip signals correctly from statistical error noise like that seen in Fig. 5(*c*). Therefore, a method for increasing the Bragg-dip signals is proposed. First, the exponent of R_{dip} is calculated. In this study we used R_{dip}^7. Fig. 5(*d*) shows how the R_{dip}^7 data increase the Bragg-dip signals and three Bragg-dip signals are identified by thresholds. The first important point of this data-analysis procedure is the exponent, which can increase the signal-to-noise ratio (see Fig. 5*d*). The other point is the odd-number exponent. An even-number exponent can increase negative values of R_{dip}. This causes an increase in the diffracted neutron noise as unphysical signals, such as those indicated in Fig. 3(*b*), and can appear in the wavelength region

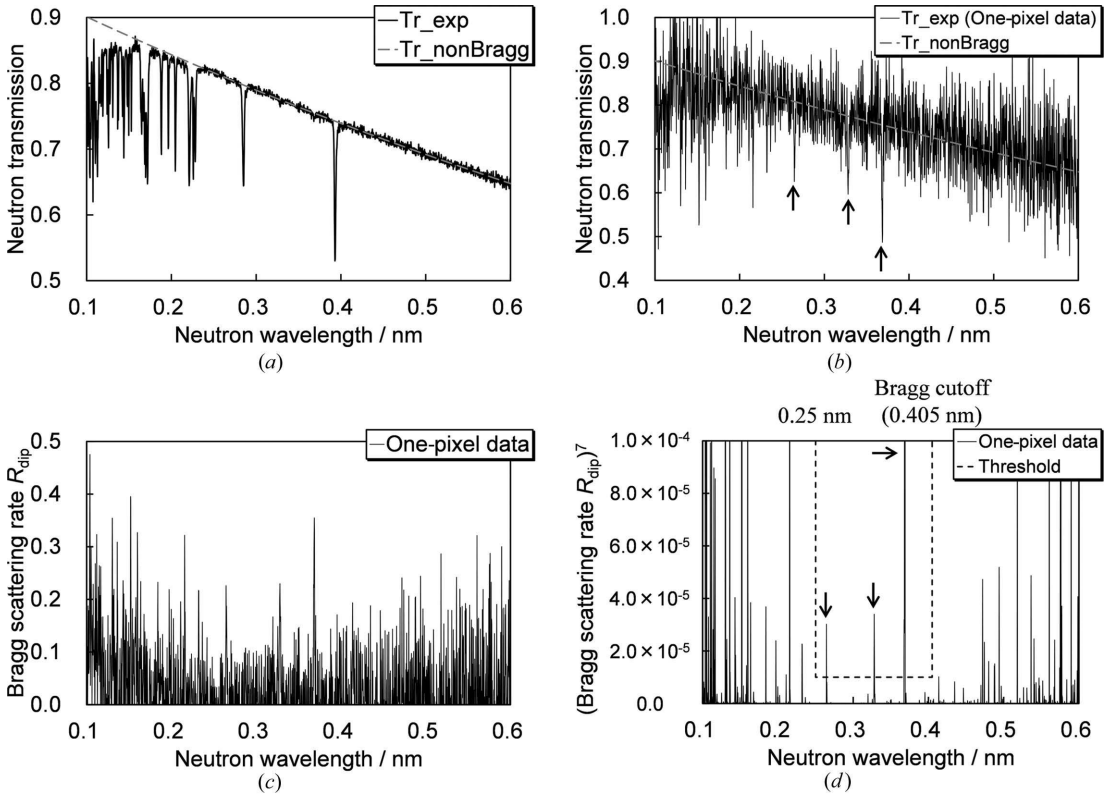

Figure 5
(*a*) An example of Tr_{exp} with high-statistics (area-integrated) data for Grain 3 and the fitted $Tr_{nonBragg}$ curve of the non-Bragg scattering baseline. (*b*) An example of Tr_{exp} of low-statistics data (one-pixel data) for Grain 1 with $Tr_{nonBragg}$. Arrows indicate Bragg-dip signals estimated from Fig. 3(*b*). (*c*) Bragg-scattering attenuation (R_{dip}) of panel (*b*). (*d*) R^7_{dip} increasing Bragg-dip signals and three Bragg-dip signals identified by the thresholds.

below 0.287 nm in the case of b.c.c. Fe. An odd-number exponent avoids this problem. The final results (neutron transmission IPF maps) using R^7_{dip} are presented in this paper, although both R^5_{dip} and R^7_{dip} usually produced the same final results. In all cases, the exponent should be suitably chosen depending on the signal-to-noise ratio of the original R_{dip} data. In this way, as Fig. 5(*d*) shows, statistical error noise is sufficiently reduced so as to be negligible.

Finally, an identification procedure of Bragg dips and their wavelengths using the R^7_{dip} data is described. Thresholds for identification levels of Bragg dips were set for both the wavelength and the intensity of the spectrum. The intensity lower level was 1.0×10^{-5}. This level should also be appropriately chosen depending on the signal-to-noise ratio of the R^7_{dip} data, as for the exponent. The wavelength lower level was 0.25 nm, this value having been chosen for two reasons as follows. At wavelengths smaller than 0.287 nm, because all Bragg dips caused by backscattering of {110} diffraction from b.c.c. Fe and some {200} Bragg dips appear, the reliability of the orientation analysis is drastically improved owing to more Bragg dips being considered. Additionally, at wavelengths greater than 0.22 nm, Bragg dips do not drastically overlap with each other (see Fig. 3*b*). Thus, the intermediate wavelength of 0.25 nm was chosen as a threshold. Actually, when this lower-threshold wavelength was set to be larger or smaller, the crystal-lattice direction determination derived incorrect orientations owing to a lack of dips, or could not derive an answer owing to drastic dip overlap, respectively. The wavelength upper level is 0.405 nm, which corresponds to the Bragg cut-off wavelength of b.c.c. Fe: Bragg dips for b.c.c. Fe do not appear above 0.405 nm. Thus, the Bragg dips within a wavelength range defined by these thresholds were investigated for each pixel. Note that these parameters are specific to the present experiment and they should be carefully and separately determined for each experiment.

4.2. Database of Bragg-dip wavelengths depending on crystal-lattice direction along the neutron transmission direction

To determine the crystal-lattice direction from the Bragg-dip wavelengths, we prepared a database of Bragg-dip wavelengths for each crystal-lattice direction. Fig. 6 shows a three-dimensional (vector) scheme of the diffraction. We aimed to identify the direction of the crystal lattice that is parallel to the neutron beam direction. We note that the identification of the crystal-lattice direction is restricted to the neutron transmission direction. It is impossible for a single-direction Bragg-dip transmission experiment to determine crystal-lattice rotation around the axis of the neutron transmission direction. For a full crystal orientation determination (not only the neutron transmission direction but also its transverse direction), it is necessary to measure and evaluate the Bragg-dip transmission

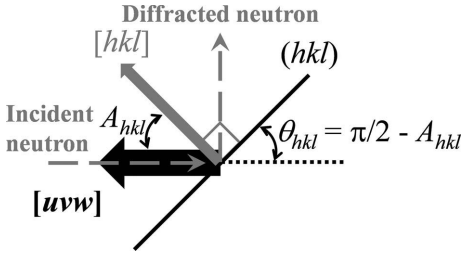

Figure 6
The three-dimensional (vector) relation between the neutron beam transmission direction (ND), the crystal-lattice direction [*uvw*] along ND, a crystal-lattice plane (*hkl*) of possible diffraction and its normal direction [*hkl*]. The [*uvw*] notation describes the crystal-lattice direction corresponding to the incident/transmitted neutron beam direction.

data from another specimen direction (Santisteban, 2005; Malamud & Santisteban, 2016).

We decided to use the crystal-lattice direction vector [*uvw*] to represent the crystal-lattice direction corresponding to the neutron transmission direction. In constructing the database all [*uvw*] are surveyed as follows: [100 100 100], [100 100 99], ..., [100 100 0], [100 99 99], [100 99 98], ..., [100 99 0], [100 98 98], ..., [100 0 0]. This corresponds to 1/8 of the orientation space. As a result, the number of possible crystal-lattice directions is 5151, as shown on the vertical axis of Fig. 7(*a*).

The Bragg-dip wavelengths for each [*uvw*] were calculated. Firstly, all the lattice planes (*hkl*) of possibly diffracting planes and their spacings d_{hkl} were derived using the known information on the crystal structure. In this study we used the structural information for b.c.c. Fe (lattice parameter 0.28665 nm). Then, the angle A_{hkl} between [*uvw*] and each [*hkl*] [the normal direction of the (*hkl*) plane] is calculated (illustrated in Fig. 6):

$$A_{hkl} = \arccos\left[\frac{hu + kv + lw}{(h^2 + k^2 + l^2)^{1/2}(u^2 + v^2 + w^2)^{1/2}}\right]. \quad (4)$$

In addition, the Bragg angle θ_{hkl} can be expressed by

$$\theta_{hkl} = \frac{\pi}{2} - A_{hkl}. \quad (5)$$

Finally, using Bragg's law,

$$\lambda = 2d_{hkl} \sin \theta_{hkl}, \quad (6)$$

all the Bragg-dip wavelengths λ for a [*uvw*] direction were calculated and recorded in the database. This procedure was repeated for all [*uvw*].

Fig. 7(*a*) shows the contents of the database, indicating the Bragg-dip wavelengths for the 5151 lattice directions, and Fig. 7(*b*) represents a portion of the database. In the case where the wavelength range of the match is set above 0.25 nm, a certain crystal-lattice direction along the neutron transmission direction is determined for a certain Bragg-dip pattern. This is achieved by both consideration of some {200} Bragg dips and a full examination of backscattering signals of {110} Bragg dips because this wavelength region includes wavelengths below $2d_{200} \sin 90^\circ$ and above $2d_{110} \sin 45^\circ$. Fig. 7(*c*) is an IPF showing the 5151 crystal-lattice directions identified by the database matching method, indicating that all crystal-lattice directions have been investigated for the neutron transmission direction. On the other hand, the identified points are non-uniformly distributed in 1/8 of the orientation space. However, this is not so important for the demonstration because the highest angular resolution is 0.27° while the lowest one is 0.57°.

4.3. Bragg-dip pattern matching between the experimental data and the database

To determine the [*uvw*] along the neutron transmission direction, a match between the experimental Bragg-dip data presented in §4.1 and the database presented in §4.2 is carried out. First, we assume a single grain exists along the neutron transmission path and, if the match is successful, its crystal-lattice direction along the neutron transmission direction is obtained. If the match is not successful a two-grain structure is assumed. Then, the match is retried. As a result, the crystal-lattice directions of the two grains are individually

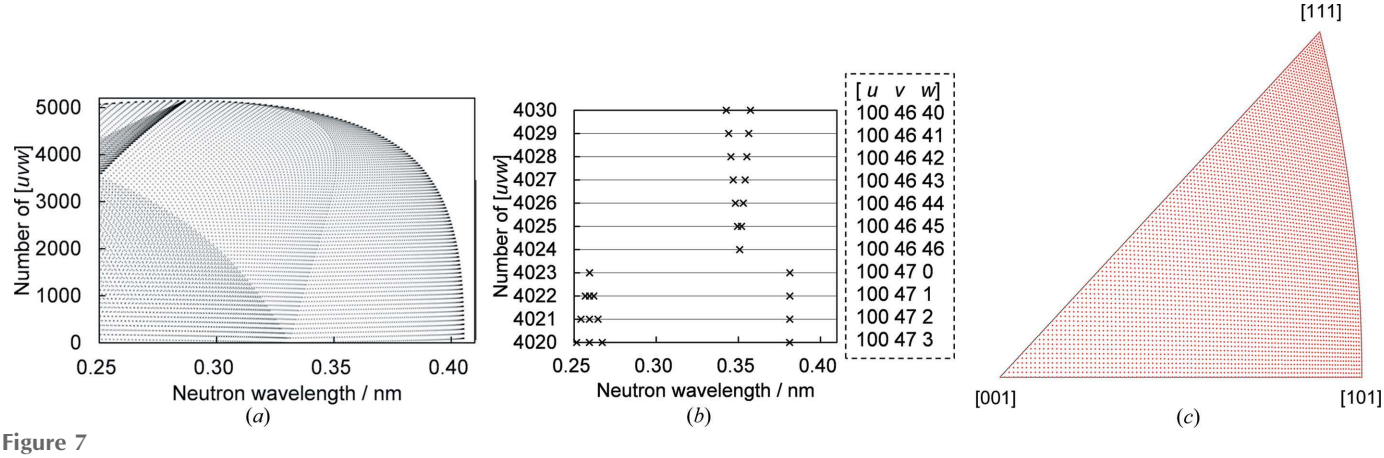

Figure 7
(*a*) 5151 patterns of Bragg-dip wavelengths for each [*uvw*]. (*b*) Enlarged section of panel (*a*) from [100 47 3] to [100 47 0] and from [100 46 46] to [100 46 40]. Cross marks (×) indicate the wavelength positions of Bragg dips. (*c*) 5151 crystal-lattice directions analysed on the inverse pole figure.

determined. If the match is not successful, three or more grains are assumed and retried. By applying this data-analysis method to the Bragg-dip transmission spectra obtained at each pixel of the imaging detector, the direction of the crystal lattice of each grain can be mapped.

A merit of this method is being able to carry out the determination of the direction of the crystal lattice quickly without any initial guess. Another merit is the ability to determine the direction of the crystal lattice of each grain, even if multiple grains are stacked in the neutron transmission path. Achieving this feature is more difficult for the least-squares whole-pattern fitting analysis methods. On the other hand, a detailed crystallographic parameter analysis like that provided by whole-pattern fitting analysis (Malamud & Santisteban, 2016) is difficult to achieve with the method presented here. Therefore, we consider that combined use of whole-pattern fitting analysis after the database matching analysis is the best approach for a detailed analysis.

5. Results of the neutron transmission IPF imaging

5.1. Results and evaluation of crystal-lattice direction analysis using the database matching method

Here, we discuss the reliability of the crystal-lattice direction obtained by the database matching method. Twelve grains were identified [their locations are shown in Fig. 10(*a*) below; see §6]. Fig. 8 shows high-statistics neutron transmission spectra obtained by integrating over the whole region of Grain 5 and Grain 9. These two grains are evaluated here because Grain 5 has the crystal-lattice direction with the smallest difference from the EBSD result and Grain 9 has the crystal-lattice direction having the largest difference from the EBSD result (see Fig. 10 and Table 1). In Fig. 8 the Bragg-dip wavelengths estimated by database matching for neutron transmission and from EBSD are plotted. The crystal-lattice directions obtained by the Bragg-dip database match unquestionably agree with the experimental Bragg-dip wavelengths, even outside the analysed wavelength range (<0.25 nm). In addition, the reliability of the database matching analysis was confirmed by the relation between the Bragg-dip depth and the indexing of the database matching method. According to the indexing (*hkl*) result of Fig. 8(*b*), two integrated Bragg dips were observed at 0.213 and 0.268 nm. The former dip consists of double dips of (211) and (21$\bar{1}$) and actually becomes deeper. The latter dip consists of triple dips of (200), (101) and (10$\bar{1}$) and actually becomes deepest. Thus, there is no contradiction between the experimental and analytical results, and it seems that the results of the crystal-lattice direction analysis of Bragg-dip neutron transmission data are correct. Incidentally, as discussed in §6.2, the EBSD results cannot identify the Bragg-dip wavelengths of the neutron transmission data.

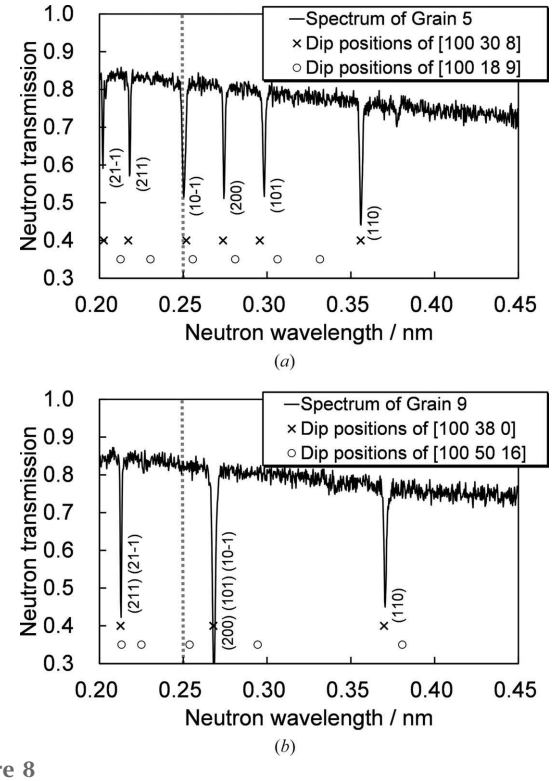

Figure 8
Area-integrated neutron transmission spectra of (*a*) Grain 5 (the minimum orientation difference from EBSD) and (*b*) Grain 9 (the maximum orientation difference from EBSD), with Bragg-dip wavelengths of the crystal-lattice direction [*uvw*] estimated from Bragg-dip neutron transmission analysis (crosses, ×) and the EBSD analysis (open circles). For the Bragg-dip neutron transmission analysis the indexing (*hkl*) results are also shown.

Table 1
Comparison between the crystal-lattice directions of Bragg-dip neutron transmission and EBSD.

Grain	Neutron transmission [*uvw*]	EBSD [*uvw*]	Angle difference (°)
1	[100 70 52]	[100 80 35]	8.52
2	[100 66 38]	[100 48 43]	8.17
3	[100 74 26]	[100 88 8]	9.65
4	[100 100 0]		
5	[100 30 8]	[100 18 9]	6.51 (minimum)
6	[100 20 0]	[100 34 7]	8.37
7	[100 43 13]	[100 35 2]	6.97
8	[100 37 37]	[100 50 50]	7.64
9	[100 38 0]	[100 50 16]	9.96 (maximum)
10	[100 17 0]	[100 30 0]	7.05
Average			8.09

5.2. Neutron transmission IPF maps

Using the database matching method, five IPF maps were obtained and these are shown in Fig. 9. Fig. 9(*b*) shows an IPF map for grains which do not overlap with another grain. The coloured regions indicate that the volume ($S \times L$) gauged by both the pixel area (S) and the neutron transmission path (L) consists of a single crystallite. Black regions are transitions between grain boundaries [*e.g.* the region between Grain 2 and Grain 3, shown in Fig. 3(*a*)] or they may be formed by a thin grain stacked on a bulky thick grain along the neutron transmission direction (*e.g.* Grain 12 stacked on Grain 3, shown in Figs. 10 and 11) or they may simply be the no-sample region (top left-hand corner). In all cases [through comparison

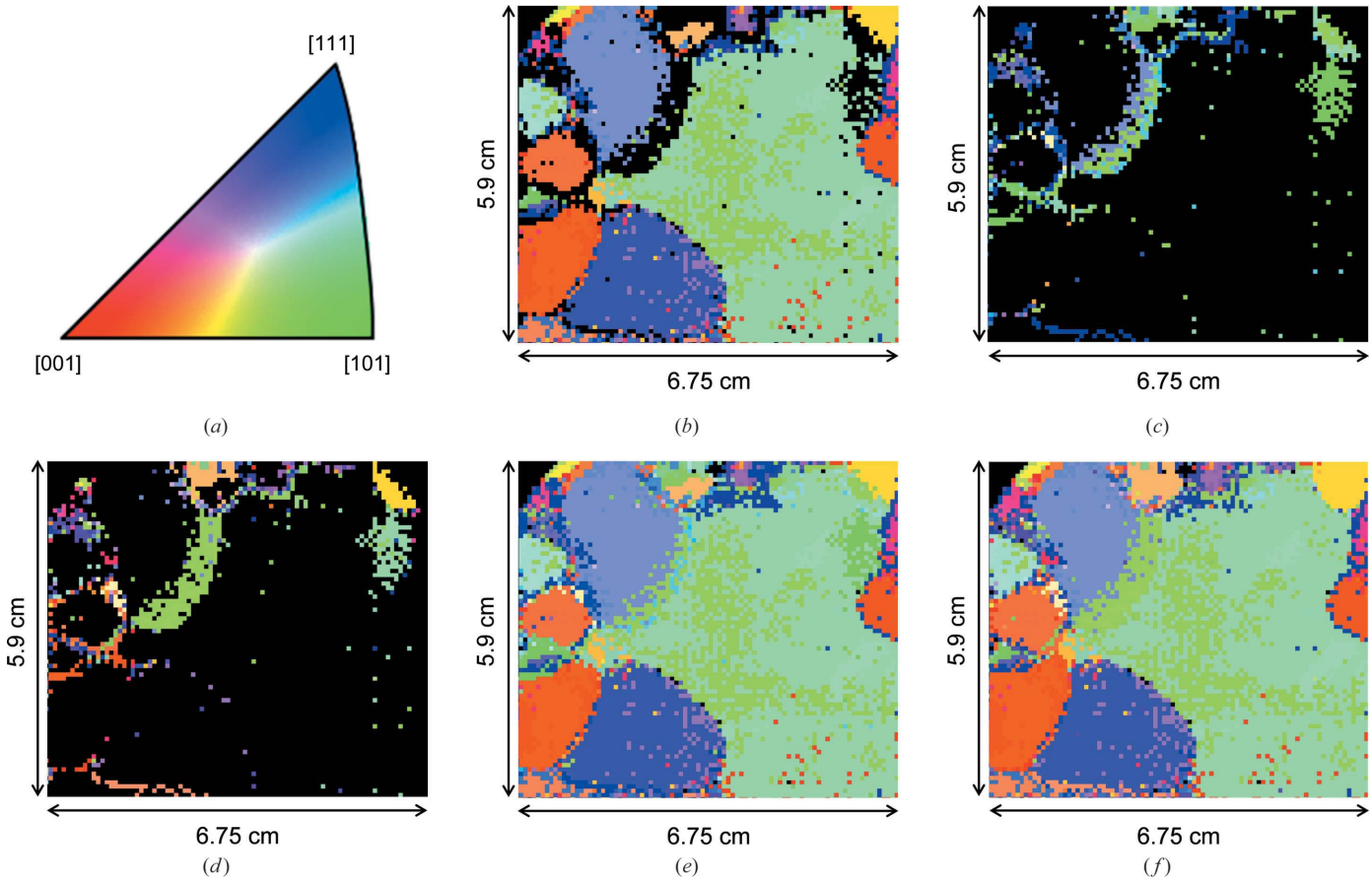

Figure 9
(*a*) Inverse pole figure (IPF) indicating the crystal-lattice direction corresponding to the neutron transmission direction. (*b*) IPF map for grains which are alone along the neutron transmission path. (*c*), (*d*) IPF maps for two grains along the neutron transmission path. (*e*) IPF map combining the maps of panels (*b*) and (*c*). (*f*) IPF map combining the maps of panels (*b*) and (*d*).

between Figs. 1 and 9(*b*)], it was confirmed that the grain shapes were well visualized using the neutron transmission method.

Figs. 9(*c*) and 9(*d*) show IPF maps for two stacked grains in the black region of Fig. 9(*b*). Fig. 9(*e*) shows a combined IPF map of Figs. 9(*b*) and 9(*c*), and Fig. 9(*f*) shows a combined IPF map of Figs. 9(*b*) and 9(*d*). Figs. 9(*e*) and 9(*f*) both indicate that the number of grains existing along the normal direction is one or two because the colour appears over the whole region except for the no-sample region. (However, a tiny region which includes three or more grains exists at the top-centre.) This was also confirmed by optical observation of the sample (see Fig. 1). Grain shapes viewed from the two sides of the plate were almost identical with only slight differences.

Thus, grain orientation imaging using Bragg-dip neutron transmission is successfully established, although the images include some statistical errors caused by low neutron counts (see Figs. 5*b* and 5*c*).

6. Comparison with EBSD

In this section, we compare the neutron transmission results with the EBSD results. Fig. 10(*a*) again shows the IPF map obtained with Bragg-dip neutron imaging (Fig. 9*e*), while Fig. 10(*b*) shows the IPF map obtained with traditional EBSD. Nine grains were identified, which were numbered according to the corresponding grains in Fig. 10(*a*). The EBSD experiments were performed at Toyohashi University of Technology using a JEOL JSM-6500F scanning electron microscope equipped with an HKL Nordlys detector. Note that 360 EBSD experiments (taking a total of nine days including sample preparation) were carried out to observe the same field of view as in neutron transmission imaging. In addition, due to the very large field of view, the working distance of EBSD (the distance between the objective lens and the sample surface, which is important for orientation analysis with constant precision because the sample is aligned in the EBSD system) gradually changed during the experiment. For this reason, the precision of the crystal-lattice directions in the EBSD scan was about $\pm 5^{\circ}$.

Comparing the images of Fig. 10, two differences become evident. One is that some grains are observed only by neutron imaging: Grains 1–3 and 5–10 are observed in both techniques, but Grains 4, 11 and 12 are observed only by neutron transmission, as discussed in §6.1. The other difference is that the grain orientations obtained by EBSD do not perfectly correspond to the orientations obtained from neutron Bragg-dip imaging. This will be discussed quantitatively in §6.2.

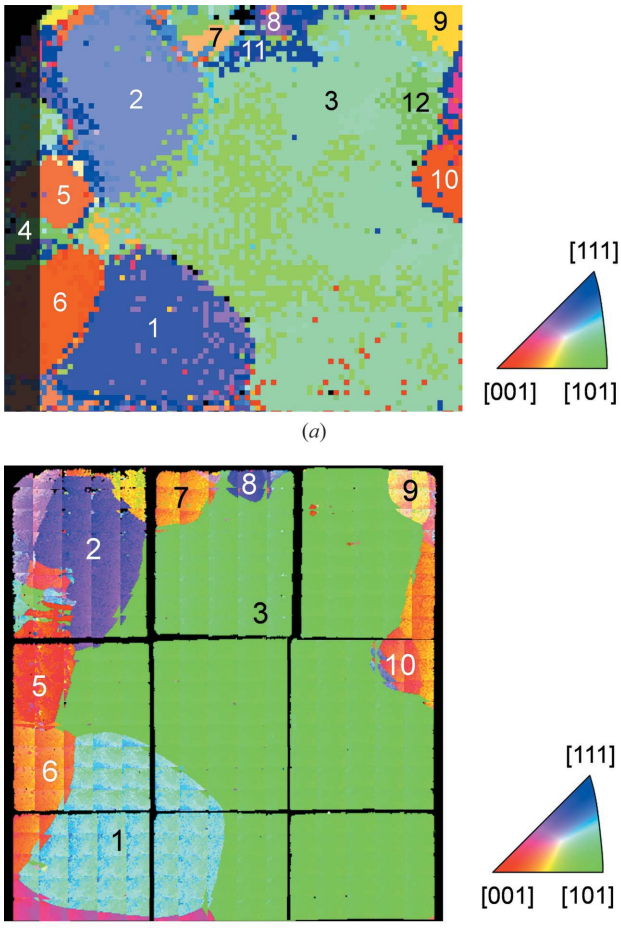

Figure 10
(*a*) IPF map obtained by Bragg-dip neutron imaging (the same as in Fig. 9*e*). (*b*) IPF map obtained by EBSD. The colours indicating the crystal-lattice directions are expressed with the same IPF definition as Fig. 9(*a*). The crystal-lattice directions evaluated by both methods are the normal directions of the sample plate (along the neutron transmission direction).

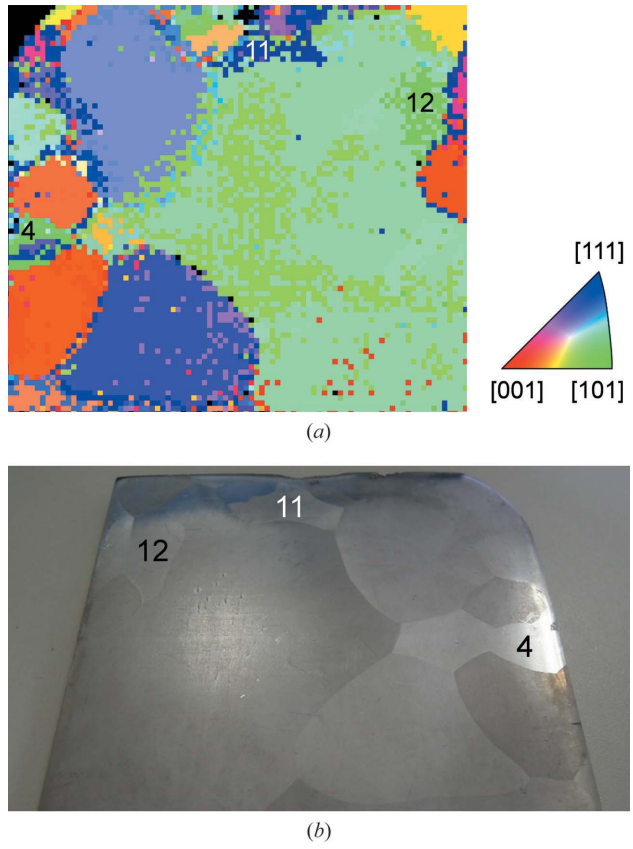

Figure 11
Comparison between the neutron transmission IPF map and the sample photograph. (*a*) Showing again the same picture as Figs. 9(*e*) and 10(*a*). (*b*) Showing again the same photograph as Fig. 1(*b*).

6.1. Differences between detected grains

Fig. 11 shows a comparison between the neutron transmission IPF map and the sample photograph. Note that the relationship between the left- and right-hand sides is reversed between these images because Fig. 11(*b*) indicates the opposite side of the surface observed by EBSD.

Grains 4, 11 and 12 are not observed by EBSD (see Fig. 10*b*). However, from Fig. 11(*b*) it is clear that these grains do actually exist. This is because EBSD can only detect surface information and cannot detect grains existing on the opposite surface of the sample plate. On the other hand, the neutron transmission method can detect grains existing not only on the opposite side but also within the bulk. This is an advantage of neutron transmission IPF mapping.

6.2. Differences in evaluated orientations

Table 1 shows the crystal-lattice directions obtained by Bragg-dip neutron imaging and EBSD, which are indicated in Fig. 10, together with their angle differences. Note that the orientation of Grain 4 was not investigated by EBSD because this grain is on the opposite side. The table shows that the difference between the two methods is about $8 \pm 2^{\circ}$. A systematic difference seems to exist. As mentioned before, the crystal-lattice directions obtained by EBSD do not reconstruct the experimental Bragg-dip wavelengths at all (see Fig. 8). This difference is caused by the fact that neutrons observe the bulk-averaged orientation, while EBSD observes the surface orientation. The orientation difference could be easily caused by sample surface-polishing conditions and sample alignment in the EBSD experiment. Thus, although the two methods give slightly different results because of the characteristics of each method, the orientation results obtained by the two methods are consistent, as shown by Fig. 10 and Table 1.

7. Conclusions

We have developed a new grain orientation mapping method using Bragg-dip neutron transmission imaging. We first developed a key data analysis of the Bragg-dip transmission spectrum by a database matching method. The database contains the Bragg-dip wavelengths for each crystal-lattice direction. By matching to the database, the number of grains included in the neutron transmission path and the direction of the crystal lattice are rapidly determined. This is more difficult with conventional laboratory methods, in particular when

analysing a material with overlapping grains. In the demonstration experiment, a position-dependent inverse pole figure map obtained by Bragg-dip neutron transmission imaging could simultaneously and correctly visualize each area and orientation of multiple grains stacked in a bulk steel plate. The advantages of the proposed method have been demonstrated, for example, the detection of grains in the bulk combined with quick and correct large-area IPF mapping.

Work in the future will include an increase in the spatial resolution of the experiment, further reduction of statistical errors, and data treatment including many Bragg dips obtained from samples with a higher number of grains (or smaller grains) and lower crystallographic symmetry. Furthermore, full determination of the crystal orientation (not only in the normal direction but also in the transverse direction) and three-dimensional tomographic mapping may be possible. Further developments in both neutron diffraction IPF imaging and neutron transmission IPF imaging will provide new opportunities for the characterization of coarse-grain-size engineering materials in actual use, *e.g.* heavy metallic materials such as electromagnetic steels and Ni-based superalloys (turbine blades).

Acknowledgements

The neutron experiment at J-PARC on the beamline MLF BL10 NOBORU was performed under a user programme (proposal No. 2014P0601). This work was supported by the ISIJ research group 'Steel microstructure analysis using compact neutron sources'.

Funding information

The following funding is acknowledged: JSPS KAKENHI (grant Nos. 23226018 and 16 K20876).

References

Cereser, A. *et al.* (2017). *Sci. Rep.* **7**, 9561.
Gutmann, M. J., Kockelmann, W., Chapon, L. C. & Radaelli, P. G. (2006). *J. Appl. Cryst.* **39**, 82–89.
Humphreys, F. J. (2004). *Scr. Mater.* **51**, 771–776.
Johnson, G., King, A., Honnicke, M. G., Marrow, J. & Ludwig, W. (2008). *J. Appl. Cryst.* **41**, 310–318.
Kockelmann, W., Frei, G., Lehmann, E. H., Vontobel, P. & Santisteban, J. R. (2007). *Nucl. Instrum. Methods Phys. Res. Sect. A*, **578**, 421–434.
Kockelmann, W., Zhang, S. Y., Kelleher, J. F., Nightingale, J. B., Burca, G. & James, J. A. (2013). *Phys. Procedia*, **43**, 100–110.
Ludwig, W., King, A., Reischig, P., Herbig, M., Lauridsen, E. M., Schmidt, S., Proudhon, H., Forest, S., Cloetens, P., du Roscoat, S. R., Buffière, J. Y., Marrow, T. J. & Poulsen, H. F. (2009). *Mater. Sci. Eng. A*, **524**, 69–76.
Ludwig, W., Schmidt, S., Lauridsen, E. M. & Poulsen, H. F. (2008). *J. Appl. Cryst.* **41**, 302–309.
Malamud, F. & Santisteban, J. R. (2016). *J. Appl. Cryst.* **49**, 348–365.
Oikawa, K., Maekawa, F., Harada, M., Kai, T., Meigo, S., Kasugai, Y., Ooi, M., Sakai, K., Teshigawara, M., Hasegawa, S., Futakawa, M., Ikeda, Y. & Watanabe, N. (2008). *Nucl. Instrum. Methods Phys. Res. Sect. A*, **589**, 310–317.
Peetermans, S., King, A., Ludwig, W., Reischig, P. & Lehmann, E. H. (2014). *Analyst*, **139**, 5765–5771.
Santisteban, J. R. (2005). *J. Appl. Cryst.* **38**, 934–944.
Santisteban, J. R., Daymond, M. R., James, J. A. & Edwards, L. (2006). *J. Appl. Cryst.* **39**, 812–825.
Santisteban, J. R., Edwards, L., Fitzpatrick, M. E., Steuwer, A., Withers, P. J., Daymond, M. R., Johnson, M. W., Rhodes, N. & Schooneveld, E. M. (2002). *Nucl. Instrum. Methods Phys. Res. Sect. A*, **481**, 765–768.
Sato, H., Kamiyama, T. & Kiyanagi, Y. (2011). *Mater. Trans.* **52**, 1294–1302.
Sato, H., Sato, T., Shiota, Y., Kamiyama, T., Tremsin, A. S., Ohnuma, M. & Kiyanagi, Y. (2015). *Mater. Trans.* **56**, 1147–1152.
Sato, H., Shiota, Y., Shinohara, T., Kamiyama, T., Ohnuma, M., Furusaka, M. & Kiyanagi, Y. (2015). *Phys. Procedia*, **69**, 349–357.
Shinohara, T., Kai, T., Oikawa, K., Segawa, M., Harada, M., Nakatani, T., Ooi, M., Aizawa, K., Sato, H., Kamiyama, T., Yokota, H., Sera, T., Mochiki, K. & Kiyanagi, Y. (2016). *J. Phys. Conf. Ser.* **746**, 012007.
Strobl, M. (2015). *Phys. Procedia*, **69**, 18–26.
Tremsin, A. S., McPhate, J. B., Steuwer, A., Kockelmann, W., Paradowska, A. M., Kelleher, J. F., Vallerga, J. V., Siegmund, O. H. W. & Feller, W. B. (2012). *Strain*, **48**, 296–305.
Uno, S., Uchida, T., Sekimoto, M., Murakami, T., Miyama, K., Shoji, M., Nakano, E., Koike, T., Morita, K., Satoh, H., Kamiyama, T. & Kiyanagi, Y. (2012). *Phys. Procedia*, **26**, 142–152.
Wenk, H.-R., Lutterotti, L. & Vogel, S. (2003). *Nucl. Instrum. Methods Phys. Res. Sect. A*, **515**, 575–588.
Woracek, R., Penumadu, D., Kardjilov, N., Hilger, A., Boin, M., Banhart, J. & Manke, I. (2014). *Adv. Mater.* **26**, 4069–4073.